PCCP

ROYAL SOCIETY OF CHEMISTRY

PAPER

View Article Online
View Journal | View Issue

Cite this: Phys. Chem. Chem. Phys., 2022, **24**, 12926

Recipes for superior ionic conductivities in thin-film ceria-based electrolytes

Dennis Kemp, *[a] Albert Tarancón [bc] and Roger A. De Souza [a]

Received 21st March 2022,
Accepted 26th April 2022

DOI: 10.1039/d2cp01335e

rsc.li/pccp

We employed Molecular Dynamics (MD) and Metropolis Monte Carlo (MMC) simulations to determine the oxide-ion mobility u_{O} in $\mathrm{Ce}_{1-y}\mathrm{Gd}_y\mathrm{O}_{2-y/2}$ (y = 0.02, 0.1, 0.2) for the range of temperatures $1400 \leq T/\mathrm{K} \leq 2000$ and field strengths $0.6 \leq E/\mathrm{MV\ cm^{-1}} \leq 15.0$. Direct, unambiguous determination of $u_{\mathrm{O}}(E)$ from MD simulations is shown to require examination of the ions' mean displacement as a function of time. MD simulations were performed for random distributions of Gd cations and equilibrium distributions obtained by MMC calculations. All $u_{\mathrm{O}}(E,T,y)$ data obtained can be described by an (empirically augmented) analytical model with four zero-field parameters, a result that allows data to be extrapolated down to the temperatures of electrolyte operation. Specifically, the oxide-ion conductivity is predicted, for example at T = 700 K, (i) to be up to 10^1 higher for a random distribution of Gd than for an equilibrium distribution; and (ii) to be a factor of $10^{0.8}$ higher for a 6 nm thin film than for a µm-thick sample under a potential difference of 1 V. By virtue of non-equilibrium deposition and nm-thick samples, thin films thus provide two new recipes for attaining even higher oxide-ion conductivities in ceria-based electrolytes.

1 Introduction

In the race from promising oxide-ion conductor to high-performance, long-lifetime, commercially viable fuel-cell electrolyte, ceria-based materials have already passed various hurdles. The thermodynamic stability under fuel cell conditions has been demonstrated, in particular for intermediate-temperature fuel cells.[1–6] The optimal phase composition has been identified in terms of the amount and type of substituent oxide, namely 10–20% of $\mathrm{Gd_2O_3}$ or $\mathrm{Sm_2O_3}$;[4,7–11] and the possibility of higher conductivity through co-substitution has been extensively studied with mixed results.[12–14] In addition, the need to avoid silicate phases at grain boundaries has been recognised[15–17] and mitigation strategies have been developed.[9,18–22]

Of the remaining hurdles, one of the most important is lowering the operation temperature in order to extend the device's lifetime. Many degradation phenomena, such as interdiffusion,[23,24] creep,[25,26] kinetic demixing,[27,28] and aging,[29–32] are governed by cation diffusion, a process characterised by a high activation enthalpy, (5 to 6) eV.[33,34] Hence, lowering the operation temperature by only 100 K leads to decreases in cation diffusion rates of six orders of magnitude, with corresponding increases in device lifetimes. Of course, oxide-ion conductivity is diminished at lower temperatures, but this can be offset by reducing the thickness of the electrolyte.[35,36]

In this study, we examined possibilities to overcome the low-temperature hurdle through the use of thin films, and to this end, we combined various simulation methods and theory. In principle, thin films provide two possibilities for increasing the oxide-ion conductivity. If a film is fabricated with a random distribution of substituent cations (by means of a physical deposition method), rather than the equilibrium distribution achieved at high temperatures of sintering, the oxide-ion conductivity should not be diminished by the formation of defect clusters or nano-domains containing multiple point defects.[37,38] In addition, if the film is thin enough, relatively small applied voltages result in extraordinarily high electric field strengths, and thus in the possibility of field-enhanced ion transport.[39–41] Field strengths of MV cm^{-1} can increase the ionic conductivity of a dilute solution of non-interacting charge carriers by orders of magnitude. The increases at such high fields for electrolyte compositions (*i.e.* well beyond the dilute limit) with either random or equilibrium Gd distributions are, however, unclear.

To examine the two possibilities of overcoming the low-temperature hurdle we performed classical molecular dynamics (MD) simulations and Metropolis Monte Carlo (MMC) simulations for three different concentrations (y = 0.02,0.1,0.2) of $\mathrm{Ce}_{1-y}\mathrm{Gd}_y\mathrm{O}_{2-y/2}$ with random and equilibrium

---

[a] *Institute of Physical Chemistry, Landoltweg 2, RWTH Aachen University, 52056 Aachen, Germany. E-mail: kemp@pc.rwth-aachen.de, desouza@pc.rwth-aachen.de; Tel: +49 241 80 98617*

[b] *Catalonia Institute for Energy Research (IREC), Jardins de Les Dones de Negre 1, 08930 Sant Adrià del Besòs, Barcelona, Spain*

[c] *ICREA, 23 Passeig Lluís Companys, Barcelona 08010, Spain*

distributions of the substituent Gd cations. For each of the six systems we obtained the oxide-ion mobility u_O as a function of field strength E and temperature T. The subsequent aim of our study was to obtain an analytical expression that describes all $u_O(E,T,y)$ data in terms of only zero-field parameters. With such an expression, the oxide-ion conductivity can be predicted, for conditions other than those examined in the simulations, with knowledge of only the bulk conductivity in the low-field limit and its activation enthalpy.

2 Theory

2.1 Obtaining field-dependent ion mobilities from MD simulations

The electrochemical mobility of a charge carrier i is defined as the ratio of the charge carrier's drift velocity ($v_{d,i}$) to the electric field strength (E) producing drift,

$$u_i = \frac{v_{d,i}}{E}. \tag{1}$$

For small E (*i.e.*, within the linear regime), u_i is independent of E. Our interest here is in the mobility within and beyond the linear regime.

The traditional approach for obtaining u_i from an MD simulation is indirect. In an isothermal MD simulation, the ions' mean-squared-displacement $\langle r_i^2\rangle$ is monitored as a function of time (t), and if the increase is smooth and linear, Einstein's relation,

$$D_i^* = \frac{1}{6}\frac{d\langle r_i^2\rangle}{dt}, \tag{2}$$

is applied to determine the tracer diffusion coefficient D_i^*. Subsequently, the Nernst–Einstein equation (with ion charge z_ie; Haven ratio H_r; and Boltzmann constant k_B)

$$u_i = \frac{|z_i|eD_i^*}{H_r k_B T} \tag{3}$$

is used to calculate the ion mobility; often $H_r = 1$ is arbitrarily assumed (*i.e.* all correlation effects[42,43] are ignored).

In the present case, this traditional approach is not applicable for two reasons. For simulations in which an applied electric field produces ion drift, the analysis of $d\langle r_i^2\rangle/dt$ does not yield D_i^*. Below we explain what the problem is, and we describe a simple and direct solution. The second reason is that, since concentrated solid solutions are considered ($Ce_{1-y}Gd_yO_{2-y/2}$ with $y > 0.01$) and high-field effects, too, H_r in eqn (3) will deviate from the (constant) dilute–solution value. That is, $H_r(E, T, y)$ would be required.

We come now to the issue of why the analysis of $d\langle r_i^2\rangle/dt$ does not yield D_i^*. For a system of ions undergoing diffusion and drift, the evolution of the ions' probability density function can be written in one dimension (x) as[44]

$$p(x,t) = \frac{1}{\sqrt{4\pi D_i^* t}}\exp\left[-\frac{(x - v_{d,i}t)^2}{4D_i^* t}\right]. \tag{4}$$

The ions' mean-squared displacement is given by the second moment of this distribution,

$$\langle x_i^2\rangle = \int_{-\infty}^{+\infty} x^2 p(x,t)dx = (v_{d,i}t)^2 + 2D_i^* t. \tag{5}$$

In the absence of drift ($v_{d,i} = 0$), eqn (5) reduces to Einstein's relation in one dimension and a linear increase in $\langle x_i^2\rangle$ with t yields the tracer diffusion coefficient. But for $v_{d,i} \neq 0$, $\langle x_i^2\rangle$ will not in general increase linearly with t and in fact, depending on $v_{d,i}$, $\langle x_i^2\rangle$ may increase according to t^2. The critical point is that $d\langle r_i^2\rangle/dt$ does not yield the tracer diffusion coefficient: it yields a quantity with a contribution from diffusion and a time-dependent contribution from drift.

Eqn (5) suggests that one solution to this problem would be to consider the second time derivative of $\langle x_i^2\rangle$ to obtain the drift velocity. We propose that a far simpler and more robust approach is to examine the ions' mean displacement, that is, the first moment of $p(x,t)$,

$$\langle x_i\rangle = \int_{-\infty}^{+\infty} x p(x,t)dx = v_{d,i}t. \tag{6}$$

In this case, a linear increase in $\langle x_i\rangle$ with t yields $v_{d,i}$; subsequently, u_i is obtained from eqn (1).

This is the approach we have used previously.[45,46] Here we present the underlying foundation because of some misconceptions in the literature. For example, in some studies,[47,48] MD simulations with an applied field ($v_{d,i} \neq 0$) were analysed with eqn (2) rather than eqn (6). This is clearly incorrect. The "diffusion coefficients" reported in such studies are no such things; consequently, the analysis of such data is unreliable, and the conclusions reached are questionable.

2.2 An analytical expression for the field-dependent ionic conductivity

The second aim of our study, as noted above, is to obtain an expression that allows the oxide-ion conductivity to be predicted for a concentrated solid solution in terms of only zero-field parameters. That is, if one had measured the bulk oxide-ion conductivity of a ceria-based material as a function of temperature, one could predict—with this knowledge and with the analytical expression—the conductivity for the high-field regime without any additional information.

The ionic conductivity is the product of the ion's mobility u_i, its charge $|z_i|e$ and its concentration c_i,

$$\sigma = u_i c_i |z_i| e. \tag{7}$$

In the present case, the electric field strengths are not large enough to generate vacancy–interstitial pairs[49] so that c_i is not a function of E. u_i, on the other hand, is affected by the applied fields and our starting point for describing this effect is the approach that has been successful for oxide-ion conduction in dilute solutions.[45,46]

The approach's underlying assumption is that the ions migrate over cosinusoidal free energy profiles, upon which the electric field is linearly superimposed.[45] The activation enthalpies of ion migration with and against the field, *i.e.* in the forward and reverse directions, follows as[45]

$$\Delta H_{\mathrm{mig}}^{\mathrm{f/r}} = \Delta H_{\mathrm{mig}}\left[\sqrt{1-\gamma^2} \mp \gamma\left(\frac{\pi}{2}\right) + \gamma \arcsin\gamma\right], \tag{8}$$

where $\gamma = (|z_i|eEd_i)/(\pi\Delta H_{\mathrm{mig}})$ with ΔH_{mig} as the activation enthalpy of ion migration in the absence of a field and d_i as the jump distance. The ions' mobility can then be expressed in terms of the difference in the rates of forward and reverse ion jumps,

$$\begin{aligned} u_i &= \frac{1}{E} n_{\mathrm{v}} d_i \nu_0 \exp\left(\frac{\Delta S_{\mathrm{mig}}}{k_{\mathrm{B}}T}\right) \\ &\quad \times \left[\exp\left(-\frac{\Delta H_{\mathrm{mig}}^{\mathrm{f}}}{k_{\mathrm{B}}T}\right) - \exp\left(-\frac{\Delta H_{\mathrm{mig}}^{\mathrm{r}}}{k_{\mathrm{B}}T}\right)\right], \end{aligned} \tag{9}$$

where the characteristic frequency ν_0 and the activation entropy of migration ΔS_{mig} are both field-independent quantities. (The site fraction of oxygen vacancies n_{v} is linked to the concentration of substituent Gd cations.)

This approach has been demonstrated[45,46] to provide a quantitative description of u_i up to relatively high field strengths. It thus indicates that the assumption of a linear field superimposed on the free energy landscape is reasonable, at least up to these fields of MV cm^{-1}. Deviations are expected for exceptionally high E, when the potential wells in which the ions sit are deformed substantially by the field, leading to field-dependent values of ν_0 and ΔS_{mig}. In addition, deviations are expected at exceptionally high E, as the electrons' distributions around the ions are significantly modified. These fields are beyond those examined in this study, however. It is noted that if accurate values of $\Delta H_{\mathrm{mig}}^{\mathrm{f/r}}$ for exceptionally high fields are required, then methods are available.[50,51] Such routes were not taken in this study, since the fields are not so high as to require such approaches, and since the primary quantity of interest (and one that can be determined experimentally) is the ion mobility. Knowledge of how the many individual barriers in such concentrated solid solutions react to an applied field would be of limited use in obtaining a macroscopic ion mobility.

3 Methods

The molecular dynamics simulations were performed using the LAMMPS code[52] with periodic boundary conditions in the *NpT* ensemble where particle number *N*, pressure *p* and temperature *T* are kept constant. To ensure this a Nosé–Hoover thermostat and barostat with damping parameters of 0.2 and 20 ps, respectively, were used.[53,54] The long-range coulombic interactions were calculated with a particle–particle particle–mesh solver[55] with an accuracy of 10^{-5}, as implemented in LAMMPS. Newton's equations of motion were integrated by means of the velocity Verlet algorithm with a timestep of 1 fs. There are several sets of potentials available in the literature for CeO_2 and Gd-substituted CeO_2, ranging from simple Buckingham-type pair potentials to more complex many-body potentials.[37,56–64] Our choice of the pair potential set was governed by three factors: reproducibility of experimental values that are important for the scope of this study, primarily the activation enthalpy of oxygen diffusion in pure CeO_2 and Gd-substituted CeO_2; robust potentials that allow MD simulations to be performed under high electric field strengths without simulation artefacts; and computationally efficient potentials that permit long, large-scale simulations with reasonable computation time. Based on studies that have already compared several sets of potentials for pure and Gd-substituted CeO_2[65,66] and on our own test simulations, we decided, therefore, to use the pair potentials reported by Minervini *et al.*[37]. These potentials have already been used in several studies to study oxide-ion conductivity and diffusion[65,67,68] as well as grain-boundary and surface segregation of dopants.[69,70] Supercells containing 12 000 ions (4000 f.u., $Ce_{4000}O_{8000}$) were used and 80, 400 or 800 Ce^{4+} ions were randomly substituted with Gd^{3+} ions to yield the intended composition of $y = 0.02$,0.1 or 0.2. The resulting charge inequality was balanced by randomly removing the appropriate number of O^{2-} ions. The three cells originated from this procedure were the starting configurations for the random distribution of GDC2, GDC10 and GDC20.

To obtain equilibrium distributions of Gd cations, two ions from a particular sublattice were picked at random and swapped; the change was accepted or rejected according to the standard Metropolis Monte Carlo (MMC) algorithm.[71] Swaps on both anion and cation sublattices were performed (alternating between the two) in order to capture the essential interactions between oxygen vacancies and acceptor-type Gd cations. Since oxygen vacancies are not real particles, they were treated as non-interacting particles without charge so that swaps with oxide ions were possible. This procedure was previously shown by Purton *et al.* to yield reasonable configurations for cation substituted supercells.[72] In the MMC minimisation, 2 × 10^6 swap attempts for anions and cations, respectively, were conducted, after which the total cell energy had decreased to a constant value. For all three concentrations the same temperature of $T = 1800$ K was used in the calculation of the acceptance rate allowing Gd cations and oxygen vacancies to reach thermodynamic equilibrium (rather than just oxygen vacancies as at lower temperature).

Oxide-ion mobilities u_{O} were determined from MD simulations with applied electric field strengths in the range of $0.6 \le E/\mathrm{MV\ cm^{-1}} \le 15.0$ by applying an additional force $F = z_i eE$ to each ion. Every simulation was first equilibrated for 75 ps followed by a production run of 3 ns for $E \le 3.0$ MV cm^{-1} or of 1 ns for $E > 3.0$ MV cm^{-1}. To improve the statistics, we performed three runs with different random number seeds for each simulation at given *E* and *T*.

4 Results

4.1 Effect of energy minimisation on Gd distribution

From MD simulations at finite temperature, we calculated the partial radial distribution functions $g_{\mathrm{Gd-O}}(r)$ and $g_{\mathrm{Gd-Gd}}(r)$ for two distributions of Gd: the random distributions (with oxygen vacancies allowed to achieve minimum energy configurations);

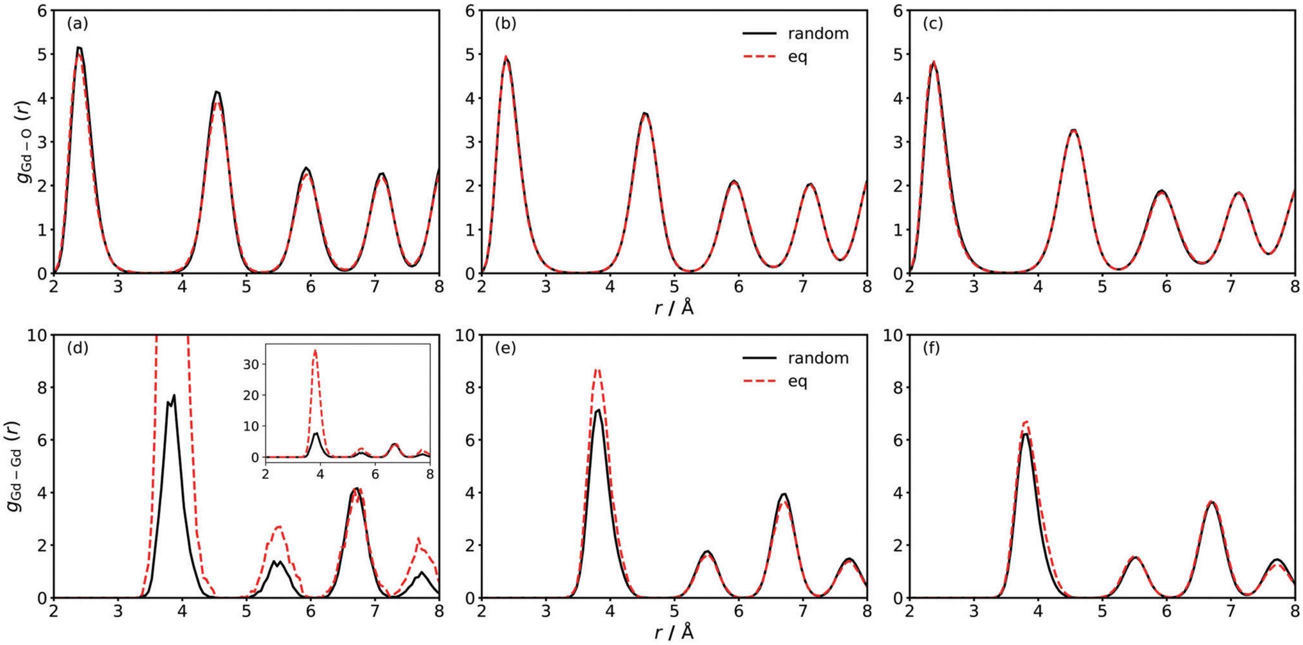

Fig. 1 Radial distribution functions for Gd–O (a–c) and Gd–Gd (d–f) of GDC2 (a and d) GDC10 (b and e) and GDC20 (c and f). Black, solid lines refer to random distributions of Gd cations and red, dashed lines refer to equilibrium distributions from Metropolis Monte Carlo (MMC) calculations. The radial distribution functions are extracted exemplarily from simulations at T = 1400 K and 0.6 MV cm^{-1} and averaged over 3000 timesteps per random seed (which sums up to 9000 timesteps per distribution) to account for different vacancy distributions. The inset in (d) shows the complete height of the first Gd–Gd peak.

and the equilibrium distributions (obtained from MMC minimisation). The results are compared in Fig. 1 for the three different systems GDC2, GDC10 and GDC20.

At first sight, $g_{\mathrm{Gd-O}}(r)$ shows no differences between random and equilibrium distributions of Gd. A closer examination reveals indeed no differences for GDC10 and GDC20, but for GDC2 $g_{\mathrm{Gd-O}}(r)$ is slightly lower for the equilibrium distribution. This indicates an increased presence of oxygen vacancies in the vicinity of Gd cations.

Substantial differences in $g_{\mathrm{Gd-Gd}}(r)$ are evident for all three compositions [Fig. 1(d)–(f)], with these differences diminishing with increasing Gd concentration. For example, in GDC2 the maximum of the 1NN peak (at 4 Å) increases from *ca.* 8 for the random distribution to *ca.* 35 upon energy minimisation [Fig. 1(d)]. Thus the probability of finding two Gd cations next to each other increases by a factor of four. A smaller but still significant increase is also observable for the 2NN (5.5 Å) and 3NN (7.8 Å) peaks, meaning that the Gd cations tend to accumulate. Combined with the observations from $g_{\mathrm{Gd-O}}(r)$ [Fig. 1(a)] it is evident that for both oxygen vacancies and Gd cations the formation of clusters is energetically favourable. Such behaviour is in agreement with theoretical and experimental studies of concentrated GDC solutions.[37,38,74–76] For GDC10 and GDC20, $g_{\mathrm{Gd-Gd}}(r)$ differs significantly between random and equilibrium distribution in the first peak only but the difference is small compared to GDC2.

These findings were obtained by averaging over the length of the simulation run but they are supported by snapshots of the simulation cells shown in Fig. 2. In the left column the random configurations (after the vacancies have achieved equilibrium) of the three concentrations and in the right column the equilibrium distributions (after the vacancies and Gd cations have achieved equilibrium) obtained from MMC simulations are shown. It is evident that in every case the equilibrium distribution has a smaller number of clusters than the corresponding random distribution. This is due to the clustering of oxygen vacancies and Gd cations with a trend to bigger clusters with increasing concentration of Gd. That is, there are more defects in the largest cluster, too.

4.2 Field-dependent oxide-ion mobilities

Oxide-ion mobilities u_{O} obtained from the MD simulations as a function of field strength are shown in Fig. 3. The qualitative behaviour of u_{O} conforms to expectations, that is, constant values in the low-field regime (up to *ca.* 2 MV cm^{-1} for the temperatures examined here), and a non-linear increase at higher field strengths. In contrast, the quantitative behaviour is quite different and does not follow the theoretical prediction (dotted lines). For example, the field strength required for an increase of $u_{\mathrm{O}}(E)/u_{\mathrm{O}}(0) = 1.1$ at $T = 1400$ K predicted by eqn (8) and (9) is $E_{\mathrm{theo}} = 3.9$ MV cm^{-1} in the case of the random GDC2 system. But from the simulation results we perceive that $E_{\mathrm{sim}} <$ 2 MV cm^{-1} is required, roughly half the expected field strength. Furthermore, for higher field strengths the deviation between theoretical prediction and simulation results becomes even larger, and it is not possible to describe the field-dependency at all regardless of the system's composition. For comparison, we note that u_{O} in a system containing only oxygen-vacancies

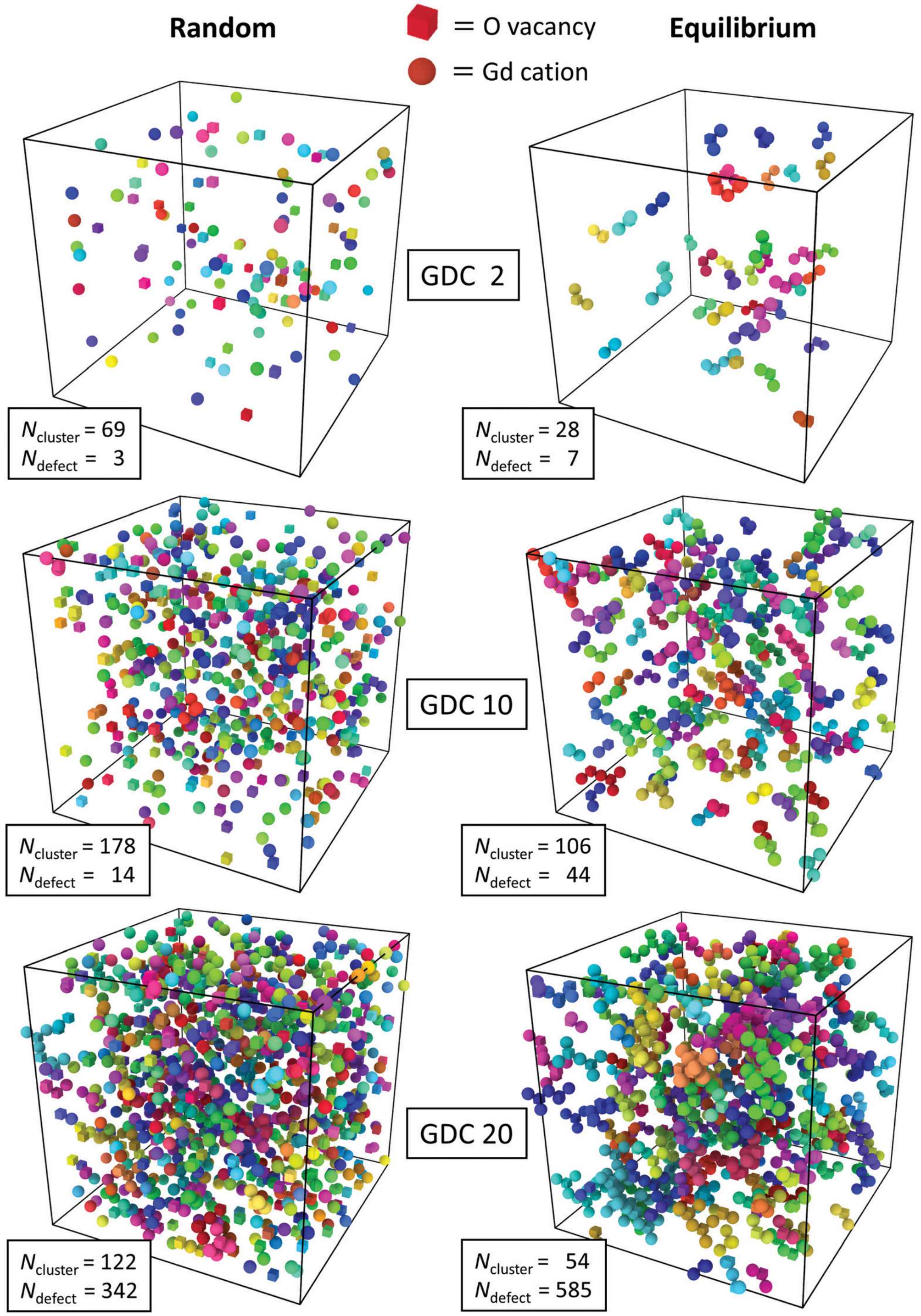

Fig. 2 Defect cluster arrangements in GDC2, GDC10 and GDC20 with random and equilibrium distributions visualized with the "Cluster Analysis" tool provided by the software OVITO.[73] Oxygen vacancies (cubes) and Gd cations (balls) with a distance of <3.5 Å belong to the same cluster and have the same colour. The number of different clusters per simulation cell, $N_{cluster}$, and the size (sum of oxygen vacancies and Gd cations) of the largest cluster, N_{defect}, is given.

(and no Gd cations) can be described by eqn (8) and (9) up to E = 20 MV cm^{-1} at T = 1400 K.[45] We attribute the deviations in Fig. 3, therefore, to the more complex energy landscape for ion-transport that the Gd substituents introduce (altered migration barriers and site energies[77,78]). As we will see in Section 5.2, a quantitative description of the field-dependent oxide-ion mobilities with a modified version of the existing model (Section 2.2) is possible.

From the oxide-ion mobilities in the low-field region ($E \leq$ 1.0 MV cm^{-1}), we extracted $u_O(T,E \rightarrow 0)$. The data are plotted in

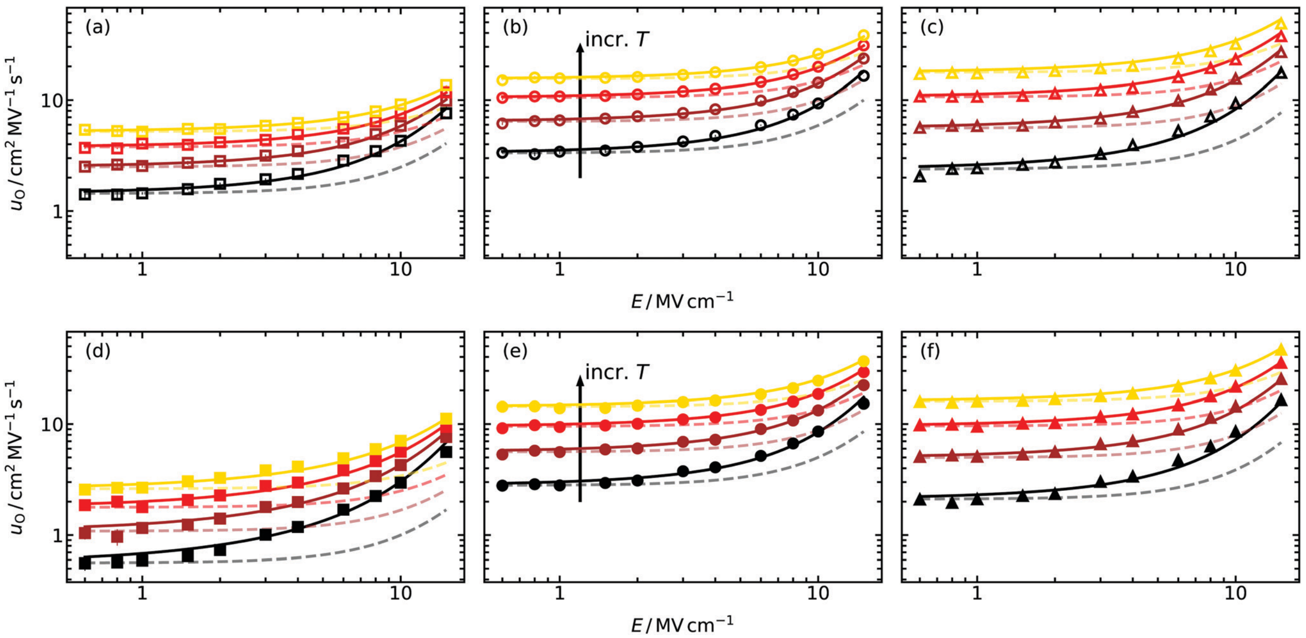

Fig. 3 Field-dependent oxide-ion mobilities u_O extracted from molecular dynamics simulations at four different temperatures (T/K = 1400, 1600, 1800, 2000) for (a and d) GDC2, (b and e) GDC10 and (c and f) GDC20. The Gd-dopant distribution in (a–c) was random, whereas in (d–f) the equilibrium distributions were employed. The solid lines are fits to the improved model [eqn (10)]; the faded, dashed lines refer to the predictions from the standard treatment[45] (Section 2.2).

Fig. 4 as a function of inverse temperature, and they yield effective enthalpies of oxygen-vacancy migration, $\Delta H_{\text{mig,v}}$. Comparing the data for random and equilibrium distributions of Gd cations, we find in the more concentrated systems, GDC10 and GDC20, that the absolute values of $u_O(T,E \rightarrow 0)$ and consequently of $\Delta H_{\text{mig,v}}$ are very similar. For GDC2, though, there is at the lowest simulated temperature already one order of magnitude difference in $u_O(T,E \rightarrow 0)$ and $\Delta H_{\text{mig,v}}$ differs by 0.1 eV. This behaviour---decreasing differences between random and equilibrium distributions of Gd with increasing Gd concentration—is a direct consequence of the defect clustering evident in Fig. 1 and 2.

5 Discussion

5.1 Influence of the cation distribution on the low-field ion mobility

For all compositions examined, the field-independent oxide-ion mobility $u_O(T,E \rightarrow 0)$ (and hence the conductivity σ) was always lower in the equilibrium case than in the random case, as reported previously for acceptor-doped fluorites.[67,72,79] The formation of larger defect clusters (Fig. 1 and 2) is accompanied by a higher binding energy[37,74,80] and a higher probability of oxygen vacancies migrating over Gd–Ce or Gd–Gd barriers (these activation barriers being much higher than the Ce–Ce barrier).[77,78] Consequently, with

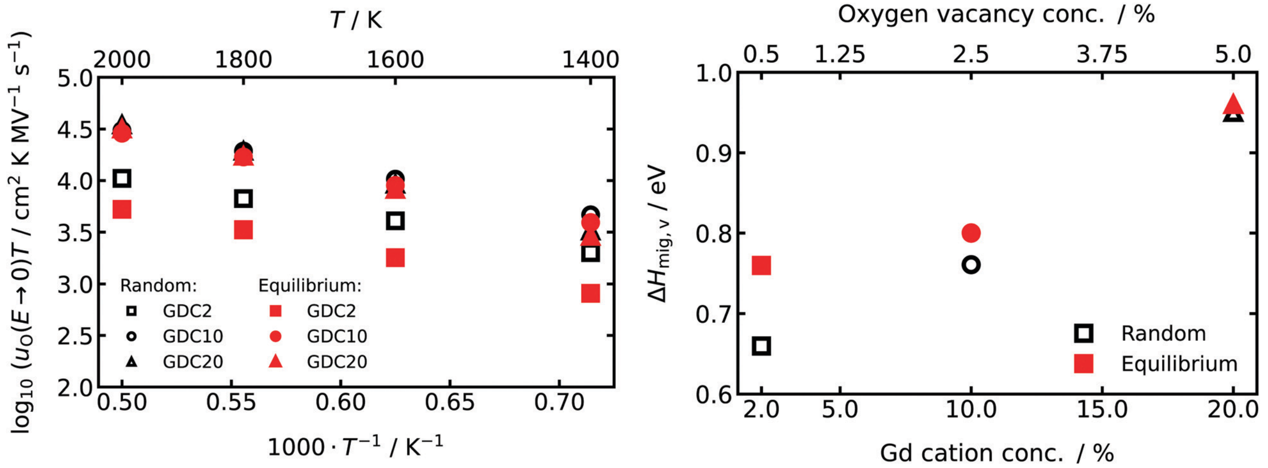

Fig. 4 (left) Field-independent oxide-ion mobilities $u(T, E \rightarrow 0)$ extrapolated from the low-field range ($E \leq 1.0$ MV cm^{-1}) of the field-dependent simulations plotted *versus* inverse temperature $1/T$. (right) Dependency of activation enthalpy of vacancy migration $\Delta H_{\text{mig,v}}$ on the concentration of Gd cations and oxygen vacancies.

increasing Gd concentration but also with larger clusters at a constant concentration of Gd, $\Delta H_{\mathrm{mig,v}}$ is expected to increase and u_{O} to decrease (Fig. 4).

Comparison of $\Delta H_{\mathrm{mig,v}}$ with values from other experimental and theoretical work reveals two findings: first, the trend of increasing activation energy (for bulk conductivity) with increasing acceptor-ion concentration was also experimentally observed for Gd-doped[10] and Sm-doped[81] $\mathrm{CeO_2}$ over a similar range of acceptor concentrations. Second, the absolute values of $\Delta H_{\mathrm{mig,v}}$ are in all cases higher than experimentally found activation energies for bulk oxide-ion conduction derived from impedance spectroscopy. For example, in GDC10 and GDC20 for $T > 623$ K, experimental activation enthalpies are in the range of 0.62–0.70 eV[9,10,16,82] and 0.74–0.82 eV,[9,10,83] respectively. In comparison the values derived from our MD simulations are 0.76/0.80 eV and 0.95/0.96 eV for the random/equilibrium distributions of GDC10 and GDC20, respectively. Theoretical studies with the same EPP derive similar $\Delta H_{\mathrm{mig,v}}$ of 0.74 eV[67] and 0.78 eV[65] for GDC8 and GDC10, respectively. As was pointed out by Grieshammer *et al.*, pair potentials tend to overestimate the repulsive and attractive interactions leading to an overestimation of the activation enthalpy.[65] Thus, with increasing Gd concentration, defect–defect interactions become increasing prevalent, thus accounting for the deviation between experimental and computational values of $\Delta H_{\mathrm{mig,v}}$ of *ca.* 0.1/0.15 eV for GDC10/GDC20. Nevertheless, the trends of the experimental values are reproduced very well by the simulations and hence a qualitative discussion of the impact of Gd distribution and high electric field strengths (see Section 5.2) on the oxide-ion mobility is possible.

5.2 Quantitative description of field-dependent oxide-ion mobilities

As already described in Section 4.2 and shown in Fig. 3, $u_{\mathrm{O}}(E,T)$ cannot be described with the standard analytical treatment (Section 2.2). At field strengths of $E > 2$ MV cm^{-1} the treatment underestimates the increase of u_{O} in all systems at all temperatures. This discrepancy is not surprising, however, considering that the treatment[45] was derived for ion migration in a simple system (low vacancy concentration, no dopant cations, and a single barrier over which ions jump). In principle, one could remedy the situation by including migration over different barrier heights (depending on the arrangement of Gd cations) and to and from sites with differing energies (depending on the arrangements of Gd cations and oxygen vacancies).[77,78,84] It is difficult to imagine, though, that a useful analytical expression would be obtained, given the huge number of possible arrangements of the defects. A simpler approach to obtain an adequate description is to adapt the existing model of eqn (9) in an *ad hoc* fashion,

$$u_i = \frac{1}{E} n_{\mathrm{v}} d_i \nu_0 \exp\left(\frac{\Delta S_{\mathrm{mig}}}{k_{\mathrm{B}}}\right) \times \left[\exp\left(-\frac{\Delta H^{\mathrm{f}}_{\mathrm{mig}}}{k_{\mathrm{B}} T}\right) - \exp\left(-\frac{\Delta H^{\mathrm{r}}_{\mathrm{mig}}}{k_{\mathrm{B}} T}\right)\right] \times \left\{1 + \frac{bE}{(k_{\mathrm{B}} T)^2}\right\}. \tag{10}$$

That is to say, we found that, by introducing a new term, $\{\ldots\}$ in eqn (10), with only one empirical parameter b, we were able to describe all $u_{\mathrm{O}}(E,T,y)$ data, as shown in Fig. 3.

The form of this term was inspired by Onsager's work on the enhanced dissociation of ion pairs in solution by an electric field.[85] Initially, we tried to apply the original formalism directly to our data, thus making the unreasonable assumption [Fig. (1) and (2)] that one can describe GDC only in terms of defect pairs (of an oxygen vacancy and a Gd cation) that dissociate more readily with increasing field strength. This approach was not successful, strongly implying that the simple picture of defect pairs is not applicable to our materials. Nevertheless, it is necessary to account for the defect–defect interactions that cause the discrepancy between the simulated mobilities and the prediction from the standard model (Fig. 3). We found that the best (but still simple) form of an additional term needs to be proportional to E/T^2 (similar to Onsager's formalism) in order to describe all our $u_{\mathrm{O}}(E,T,y)$ data.

An even stronger result is that a single value of $b = (1.1 \pm 0.2) \times 10^{-3}$ cm MV^{-1} eV^{-2} is able to describe $u_{\mathrm{O}}(E,T)$ for all three random configurations and the equilibrium configurations of GDC10 and GDC20, as shown in Fig. 3(a)–(c) and (e), (f) with the solid lines. Only the equilibrium system of GDC2 [Fig. 3(d)] needs a higher value of $b = 3.0 \times 10^{-3}$ cm MV^{-1} eV^{-2} to describe the entire data.

The reason for the difference is that oxygen vacancies in equilibrium GDC2 were far less likely to encounter Gd cations during a simulation at high fields. That is, once they broke free of a cluster (and almost every oxygen vacancy was bound in a cluster with two Gd cations, see Fig. 2), the oxygen vacancies execute jumps in an almost pure $\mathrm{CeO_2}$ matrix, since there aren't that many Gd cations and those that are present are clustered together. Indeed, extracting the average number of Gd cations with full 1NN and 2NN oxygen shells (*i.e.* no oxygen vacancies present) from the MD simulations, and plotting this data as a function of field strength in Fig. 5, we find that equilibrium GDC2 is the only composition that shows different behaviour,

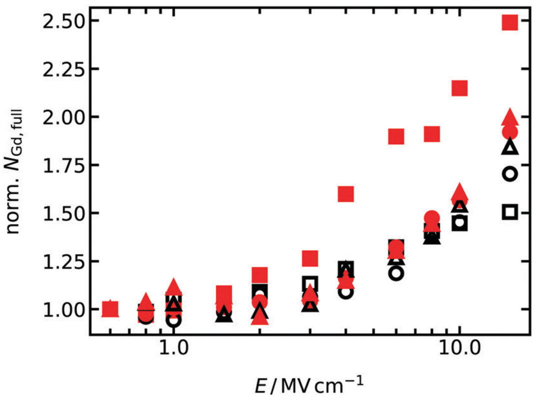

Fig. 5 Average number of Gd cations with fully occupied 1NN and 2NN shells of oxide ions, $N_{\mathrm{Gd,full}}$, for T = 1400 K. For better comparison between all concentrations and cation distributions, the number of Gd cations are normalised to the value at the lowest field strength. Meaning of the symbols is the same as in Fig. 4.

namely, a strong increase in the number of oxygen vacancies not bound to Gd cations with increasing field. Thus, not only can the difference be explained, but also the higher value found for *b*.

5.3 Prediction of field-dependent oxide-ion mobilities for thin-film electrolytes

The description of the entire set of data for all systems in Section 5.2 allows us further to predict oxide-ion mobilities, and subsequently conductivities, for other temperatures and field strengths of interest. In Fig. 6 we show calculated σ for all three concentrations in random as well as equilibrium configuration for T = 700 K and field strengths of $E = 10^{-2}$–10^{1} MV cm^{-1}. This is a typical temperature in the application of IT-SOFCs, and importantly, it is above the temperature range at which a change in enthalpy is often observed experimentally.[84]

The predictions show that at low field strengths the highest σ are achieved for the random configurations of GDC2 and GDC10. The conductivity for GDC20 at the same T and E is almost one order of magnitude lower due to the higher migration enthalpy (see Section 5.2). σ is always lower in the equilibrium case than in the random case for all three concentrations. Therefore, achieving the highest conductivities involves a random distribution of cations in the sample being produced through physical deposition of a thin film (by, *e.g.*, pulsed laser deposition or sputtering) and being maintained by avoiding high temperatures. Also plotted in Fig. 6 (on the top abscissa axis) is the thickness of a hypothetical thin-film electrolyte that corresponds to the electric field strength E when a voltage of one volt is applied. (Data are plotted down to a film thickness of five nm.) In this way, we show that thin films of physically reasonable thicknesses (*i.e.* much greater than a unit cell) with a physically reasonable applied voltage (1 V) are predicted to exhibit field-accelerated conductivities, with increases being at least twice as high as in the low-field regime. For an increase of one order of magnitude at this temperature, the film thickness would need to be in the range of only a few nanometres already approaching the unit cell limit. And voltages of 10 V will decompose the oxide.

It needs to be emphasised that the experimental conductivity behaviour of thin ceria films may be affected by a host of other phenomena. Lattice strain introduced during film preparation can be beneficial or detrimental to ionic conductivity;[86–88] microstructural features such as grain boundaries can decrease the ionic conductivity.[89–93] Thus, carefully conducted measurements as a function of field strength and temperature are needed to safely distinguish field-enhanced ion transport from other effects.[45,94,95]

5.4 Field-dependent oxide-ion mobilities for resistive switching applications

There is a second application for which the field- and temperature-dependent behaviour of the ion mobility in oxides plays a central role: resistive switching random access memory (ReRAM), an energy-efficient, high-density, non-volatile possibility for information storage. Upon application of a few volts to a ReRAM oxide, its resistance should switch within nanoseconds between low- and high-resistance states (the write step), but upon repeated application of voltages of a fraction of a volt (the read step), the resistance state should remain unchanged. One source of such extreme non-linearity is $u_{\mathrm{O}}(E,T)$.[96]

The main contenders for the active ReRAM oxide are un-doped binary systems, HfO_2 and Ta_2O_5. Systems such as $Ce_{1-y}Gd_yO_{2-y/2}$ understandably have not received much attention,[97] because the changes in defect concentrations upon

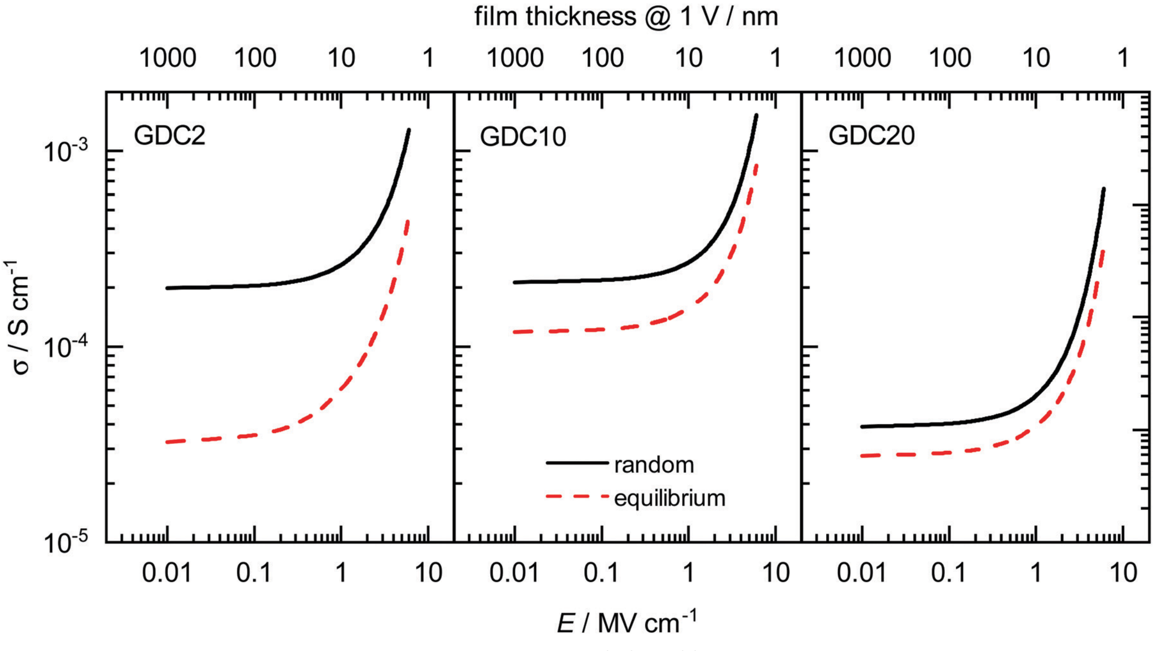

Fig. 6 Field-dependent ionic conductivities σ at T = 700 K calculated with eqn (10) and (7) for all three concentrations with random as well as equilibrium distributions of Gd. The corresponding thickness of a hypothetical thin film at an applied voltage of 1 V is shown on the top abscissa axis.

switching are rather modest, and this leads to unstable resistance states over longer times (the written information does not stay written). What our results show (Fig. 3) is that $Ce_{1-y}Gd_yO_{2-y/2}$ systems have higher non-linearity than the pure oxide, and we attribute this to the defect–defect interactions (see Sections 5.1 and 5.2 for details). Such systems, due to their high non-linearity and ability to forget, may be suitable for application in neuromorphic computing.

6 Conclusions

We suggested two new recipes for ceria-based electrolytes to overcome the low-temperature hurdle in the race from promising ion-conductor to a high-performance fuel-cell electrolyte. Through a combination of MD and MMC calculations, we obtained oxide-ion mobilities as a function of temperature and field strength for three different $Ce_{1-y}Gd_yO_{2-y/2}$ systems and two different Gd distributions (random and equilibrium). Five key messages are emphasized:

- Obtaining (field-dependent) ion mobilities from MD simulations must involve the analysis of the ions' time-dependent mean displacement rather than their mean-squared displacement.
- The distribution of substituent cations has a substantial effect on the oxide-ion mobility u_O and its activation enthalpy at low cation concentrations but these effects diminish with increasing Gd concentration.
- The standard analytical treatment for field-dependent ion mobility is not applicable for solid solutions due to defect–defect interactions, but an empirical augmentation of this model with one additional parameter yields a quantitative description of all $u_O(E,T,y)$ data obtained in this study.
- The increased non-linearity of u_O at high electric fields in $Ce_{1-y}Gd_yO_{2-y/2}$ compared with pure ceria suggests that the introduction of interacting defects in such materials may be beneficial for the application in neuromorphic computing.
- Predicted oxide-ion conductivities for $T = 700$ K, a typical IT-SOFC working temperature, indicate that the combination of thin films with thickness <10 nm and random instead of equilibrium Gd distribution can increase oxide-ion conductivity of ceria–gadolinia materials by more than one order of magnitude.

Author contributions

The project was initiated by R. A. D. S. and A. T. Simulations were performed and analysed by D. K. Data analysis and interpretation was carried out by D. K. under the supervision of R. A. D. S. The paper was written by D. K. and R. A. D. S., with support from A. T.

Conflicts of interest

There are no conflicts to declare.

Acknowledgements

Funding from the German Research Foundation (DFG) within the framework of the collaborative research center SFB 917 (Nanoswitches) is acknowledged. This project received funding from the European Union's Horizon 2020 research and innovation program under grant agreement no. 101017709 (EPISTORE). Simulations were performed with computing resources granted by RWTH Aachen University under Project No. rwth0517 and rwth0656. We thank G. F. Harrington and R. Dittmann for helpful discussions.

Notes and references

1 H. L. Tuller and A. S. Nowick, *J. Electrochem. Soc.*, 1975, **122**, 255–259.
2 H. Yahiro, Y. Baba, K. Eguchi and H. Arai, *J. Electrochem. Soc.*, 1988, **135**, 2077–2080.
3 M. Sahibzada, B. C. H. Steele, K. Zheng, R. A. Rudkin and I. S. Metcalfe, *Catal. Today*, 1997, **38**, 459–466.
4 H. Yahiro, K. Eguchi and H. Arai, *Solid State Ionics*, 1989, **36**, 71–75.
5 R. Doshi, V. L. Richards, J. D. Carter, X. Wang and M. Krumpelt, *J. Electrochem. Soc.*, 1999, **146**, 1273–1278.
6 B. Dalslet, P. Blennow, P. V. Hendriksen, N. Bonanos, D. Lybye and M. Mogensen, *J. Solid State Electrochem.*, 2006, **10**, 547–561.
7 K. Eguchi, T. Setoguchi, T. Inoue and H. Arai, *Solid State Ionics*, 1992, **52**, 165–172.
8 H. Inaba and H. Tagawa, *Solid State Ionics*, 1996, **83**, 1–16.
9 B. C. H. Steele, *Solid State Ionics*, 2000, **129**, 95–110.
10 Z. Tianshu, P. Hing, H. Huang and J. A. Kilner, *Solid State Ionics*, 2002, **148**, 567–573.
11 J. Koettgen, S. Grieshammer, G. Dück, G. Ulbrich, M. Lerch and M. Martin, *Solid State Ionics*, 2020, **355**, 115422.
12 D. Maricle, T. Swarr and S. Karavolis, *Solid State Ionics*, 1992, **52**, 173–182.
13 J. M. Ralph, J. A. Kilner and B. C. H. Steele, *MRS Proc.*, 1999, **575**, 309–314.
14 A. V. Coles-Aldridge and R. T. Baker, *Solid State Ionics*, 2020, **347**, 115255.
15 R. Gerhardt and A. S. Nowick, *J. Am. Ceram. Soc.*, 1986, **69**, 641–646.
16 X.-D. Zhou, W. Huebner, I. Kosacki and H. Anderson, *J. Am. Ceram. Soc.*, 2002, **85**, 1757–1762.
17 X. Guo, W. Sigle and J. Maier, *J. Am. Ceram. Soc.*, 2003, **86**, 77–87.
18 S. Badwal, *Solid State Ionics*, 1998, **109**, 167–186.
19 J. Drennan, *Solid State Ionics*, 2000, **134**, 75–87.
20 J. Lane, J. Neff and G. Christie, *Solid State Ionics*, 2006, **177**, 1911–1915.
21 T. S. Zhang, J. Ma, S. H. Chan, P. Hing and J. A. Kilner, *Solid State Sci.*, 2004, **6**, 565–572.
22 T. Zhang, *Solid State Ionics*, 2004, **167**, 203–207.
23 A. Tsoga, A. Naoumidis, A. Gupta and D. Stöver, *Mater. Sci. Forum*, 1999, **308-311**, 794–799.

24 Z.-P. Li, T. Mori, G. J. Auchterlonie, J. Zou and J. Drennan, *J. Solid State Chem.*, 2011, **184**, 2458–2461.

25 F. Iguchi, Y. Endo, T. Ishida, K. Sato, T. Hashida and H. Yugami, Solid State Ionics: The Science and Technology of Ions in Motion – Proceedings of the 9th Asian Conference, 2004, pp. 179–186.

26 J. L. Routbort, K. C. Goretta, A. R. de Arellano-López and J. Wolfenstine, *Scr. Mater.*, 1997, **38**, 315–320.

27 M. Martin and O. Schulz, Solid State Ionics: The Science and Technology of Ions in Motion – Proceedings of the 9th Asian Conference, 2004, pp. 787–797.

28 G. Petot-Ervas and C. Petot, *Ionics*, 2005, **11**, 189–197.

29 T. S. Zhang, J. Ma, H. T. Huang, P. Hing, Z. T. Xia, S. H. Chan and J. A. Kilner, *Solid State Sci.*, 2003, **5**, 1505–1511.

30 T. S. Zhang, J. Ma, L. B. Kong, S. H. Chan and J. A. Kilner, *Solid State Ionics*, 2004, **170**, 209–217.

31 M. Yan, T. Mori, J. Zou, G. J. Auchterlonie and J. Drennan, *J. Eur. Ceram. Soc.*, 2010, **30**, 2505–2513.

32 R. Fuentes and R. Baker, *Int. J. Hydrogen Energy*, 2008, **33**, 3480–3484.

33 S. Beschnitt, T. Zacherle and R. A. De Souza, *J. Phys. Chem. C*, 2015, **119**, 27307–27315.

34 S. Beschnitt and R. A. De Souza, *Solid State Ionics*, 2017, **305**, 23–29.

35 E. Gourba, P. Briois, A. Ringuedé, M. Cassir and A. Billard, *J. Solid State Electrochem.*, 2004, **8**, 633–637.

36 H. Huang, T. M. Gür, Y. Saito and F. Prinz, *Appl. Phys. Lett.*, 2006, **89**, 143107.

37 L. Minervini, M. O. Zacate and R. W. Grimes, *Solid State Ionics*, 1999, **116**, 339–349.

38 D. R. Ou, T. Mori, F. Ye, J. Zou, G. Auchterlonie and J. Drennan, *Phys. Rev. B: Condens. Matter Mater. Phys.*, 2008, **77**, 024108.

39 E. Verwey, *Physica*, 1935, **2**, 1059–1063.

40 J. Frenkel, *Kinetic Theory of Liquids*, Oxford University Press, Oxford, 1946.

41 N. F. Mott and R. W. Gurney, *Electronic Processes in Ionic Crystal*, Oxford University Press, Oxford, 2nd edn, 1950.

42 G. Murch, *Solid State Ionics*, 1982, **7**, 177–198.

43 H. J. D. Bruin and G. E. Murch, *Philos. Mag.*, 1973, **27**, 1475–1488.

44 M. Schroeder and M. Martin, *Z. Phys. Chem.*, 1998, **207**, 1–19.

45 A. R. Genreith-Schriever and R. A. De Souza, *Phys. Rev. B*, 2016, **94**, 224304.

46 D. Kemp and R. A. De Souza, *Phys. Rev. Mater.*, 2021, **5**, 105401.

47 M. S. Abdallah and M. Youssef, *Phys. Rev. Mater.*, 2021, **5**, 114606.

48 W. Xu, A. Maksymenko, S. Hasan, J. J. Meléndez and E. Olevsky, *Acta Mater.*, 2021, **206**, 116596.

49 M. Schie, S. Menzel, J. Robertson, R. Waser and R. A. De Souza, *Phys. Rev. Mater.*, 2018, **2**, 035002.

50 A.-M. El-Sayed, M. B. Watkins, T. Grasser and A. L. Shluger, *Phys. Rev. B*, 2018, **98**, 064102.

51 N. Salles, L. Martin-Samos, S. de Gironcoli, L. Giacomazzi, M. Valant, A. Hemeryck, P. Blaise, B. Sklenard and N. Richard, *Nat. Commun.*, 2020, **11**, 3330.

52 A. P. Thompson, H. M. Aktulga, R. Berger, D. S. Bolintineanu, W. M. Brown, P. S. Crozier, P. J. In't Veld, A. Kohlmeyer, S. G. Moore, T. D. Nguyen, R. Shan, M. J. Stevens, J. Tranchida, C. Trott and S. J. Plimpton, *Comput. Phys. Commun.*, 2022, **271**, 108171.

53 S. Nosé, *J. Chem. Phys.*, 1984, **81**, 511–519.

54 W. G. Hoover, *Phys. Rev. A: At., Mol., Opt. Phys.*, 1985, **31**, 1695–1697.

55 R. W. Hockney, *Computer simulation using particles*, CRC Press, Boca Raton, 1988.

56 V. Butler, C. Catlow, B. Fender and J. Harding, *Solid State Ionics*, 1983, **8**, 109–113.

57 M. W. D. Cooper, M. J. D. Rushton and R. W. Grimes, *J. Phys.: Condens. Matter*, 2014, **26**, 105401.

58 A. Gotte, D. Spangberg, K. Hermansson and M. Baudin, *Solid State Ionics*, 2007, **178**, 1421–1427.

59 A. Gotte, K. Hermansson and M. Baudin, *Surf. Sci.*, 2004, **552**, 273–280.

60 R. W. Grimes, G. Busker, M. A. McCoy, A. Chroneos, J. A. Kilner and S.-P. Chen, *Ber. Bunsen-Ges.*, 1997, **101**, 1204–1210.

61 A. Pedone, G. Malavasi, M. C. Menziani, A. N. Cormack and U. Segre, *J. Phys. Chem. B*, 2006, **110**, 11780–11795.

62 T. Sayle, S. Parker and C. Catlow, *Surf. Sci.*, 1994, **316**, 329–336.

63 T. X. T. Sayle, M. Molinari, S. Das, U. M. Bhatta, G. Möbus, S. C. Parker, S. Seal and D. C. Sayle, *Nanoscale*, 2013, **5**, 6063.

64 S. Vyas, R. W. Grimes, D. H. Gay and A. L. Rohl, *J. Chem. Soc., Faraday Trans.*, 1998, **94**, 427–434.

65 S. Grieshammer, L. Momenzadeh, I. Belova and G. E. Murch, *Solid State Ionics*, 2020, **355**, 115424.

66 H. Xu, R. K. Behera, Y. Wang, F. Ebrahimi, S. B. Sinnott, E. D. Wachsman and S. R. Phillpot, *Solid State Ionics*, 2010, **181**, 551–556.

67 A. Tarancón, A. Morata, F. Peiró and G. Dezanneau, *Fuel Cells*, 2010, **11**, 26–37.

68 J. A. Purton, *Phys. Chem. Chem. Phys.*, 2019, **21**, 9802–9809.

69 G. Arora and D. S. Aidhy, *J. Mater. Chem. A*, 2017, **5**, 4026–4035.

70 H. B. Lee, F. B. Prinz and W. Cai, *Acta Mater.*, 2013, **61**, 3872–3887.

71 N. Metropolis, A. W. Rosenbluth, M. N. Rosenbluth, A. H. Teller and E. Teller, *J. Chem. Phys.*, 1953, **21**, 1087–1092.

72 J. A. Purton, N. L. Allan and D. S. D. Gunn, *Solid State Ionics*, 2017, **299**, 32–37.

73 A. Stukowski, *Modell. Simul. Mater. Sci. Eng.*, 2010, **18**, 015012.

74 Z.-P. Li, T. Mori, F. Ye, D. Ou, J. Zou and J. Drennan, *J. Chem. Phys.*, 2011, **134**, 224708.

75 P. A. Žguns, A. V. Ruban and N. V. Skorodumova, *Phys. Chem. Chem. Phys.*, 2017, **19**, 26606–26620.

76 P. A. Žguns, A. V. Ruban and N. V. Skorodumova, *Phys. Chem. Chem. Phys.*, 2018, **20**, 11805–11818.

77 S. Grieshammer, B. O. H. Grope, J. Koettgen and M. Martin, *Phys. Chem. Chem. Phys.*, 2014, **16**, 9974.

78 M. Nakayama and M. Martin, *Phys. Chem. Chem. Phys.*, 2009, **11**, 3241.

79 S. Vives, D. Ramel and C. Meunier, *Ceram. Int.*, 2019, **45**, 21625–21634.

80 F. Ye, T. Mori, D. Ou, A. Cormack, R. Lewis and J. Drennan, *Solid State Ionics*, 2008, **179**, 1962–1967.

81 J. Koettgen and M. Martin, *J. Am. Ceram. Soc.*, 2020, **103**, 3776–3787.

82 B. Li, X. Wei and W. Pan, *Int. J. Hydrogen Energy*, 2010, **35**, 3018–3022.

83 L. Chen, C. L. Chen, D. X. Huang, Y. Lin, X. Chen and A. J. Jacobson, *Solid State Ionics*, 2004, **175**, 103–106.

84 J. Koettgen, S. Grieshammer, P. Hein, B. O. H. Grope, M. Nakayama and M. Martin, *Phys. Chem. Chem. Phys.*, 2018, **20**, 14291–14321.

85 L. Onsager, *J. Chem. Phys.*, 1934, **2**, 599–615.

86 R. A. De Souza, A. Ramadan and S. Hörner, *Energy Environ. Sci.*, 2012, **5**, 5445–5453.

87 G. F. Harrington, L. Sun, B. Yildiz, K. Sasaki, N. H. Perry and H. L. Tuller, *Acta Mater.*, 2019, **166**, 447–458.

88 G. F. Harrington, S. Kim, K. Sasaki, H. L. Tuller and S. Grieshammer, *J. Mater. Chem. A*, 2021, **9**, 8630–8643.

89 D. S. Mebane and R. A. De Souza, *Energy Environ. Sci.*, 2015, **8**, 2935–2940.

90 G. F. Harrington, A. Cavallaro, D. W. McComb, S. J. Skinner and J. A. Kilner, *Phys. Chem. Chem. Phys.*, 2017, **19**, 14319–14336.

91 D. V. Laethem, J. Deconinck, D. Depla and A. Hubin, *J. Eur. Ceram. Soc.*, 2016, **36**, 1983–1994.

92 X. Tong, D. S. Mebane and R. A. De Souza, *J. Am. Ceram. Soc.*, 2019, **103**, 5–22.

93 D. V. Laethem, J. Deconinck and A. Hubin, *J. Eur. Ceram. Soc.*, 2020, **40**, 2404–2416.

94 S. Murugavel and B. Roling, *J. Non-Cryst. Solids*, 2005, **351**, 2819–2824.

95 A. Heuer, S. Murugavel and B. Roling, *Phys. Rev. B: Condens. Matter Mater. Phys.*, 2005, **72**, 174304.

96 S. Menzel, M. von Witzleben, V. Havel and U. Böttger, *Faraday Discuss.*, 2019, **213**, 197–213.

97 R. Schmitt, J. Spring, R. Korobko and J. L. M. Rupp, *ACS Nano*, 2017, **11**, 8881–8891.